



Carbon electrode materials for supercapacitors obtained by co-carbonization of coal-tar pitch and sawdust

Xingyu Meng¹, Qing Cao^{1,*}, Li'e Jin¹, Xiaohua Zhang¹, Shilei Gong¹, and Ping Li¹

¹ College of Chemistry and Chemical Engineering, Taiyuan University of Technology, Taiyuan, 030024, China

Received: 11 July 2016

Accepted: 2 September 2016

Published online:
9 September 2016

© Springer Science+Business
Media New York 2016

ABSTRACT

High-surface area-activated carbons (ACs) are successfully prepared by coal-tar pitch (CTP)/sawdust (SD) co-carbonization followed by simple KOH activation. The ACs inherit the tubular morphology of the biomass and possess a hierarchical porous structure, a high specific surface area of 2224 m²/g, and a considerable amount of oxygen-containing species on the surface. The AC obtained from the co-carbonization of 67 % CTP and 33 % SD has a 25 wt% higher oxygen content than the AC (0.17 wt%) from 100 % CTP, and has a 27.50 wt% higher carbon yield than the AC (14.42 wt%) from SD. As an electrode material for supercapacitors, the prepared electrode from 67 % CTP and 33 % SD exhibits a favorable specific capacitance of 251 F/g at a current density of 0.5 A/g in 6 mol/L KOH electrolyte. The electrode also demonstrates excellent cycling stability with a retention rate of 93 % over 7000 cycles at 2 A/g and a favorable rate capability with a retention rate of 74 % when the current density increases from 0.5 to 5 A/g. Therefore, the ACs obtained by co-carbonizing CTP and SD have high potential as electrode materials. This route not only enhances the benefit from agricultural wastes, but also reduces the cost of producing electrode materials for supercapacitors.

Introduction

Energy production and utilization are critical to rapid economic development in both the past and the future [1–3]. Given the increasing energy storage requirements of the electrically driven modern world, supercapacitors have received increasing attention and have been used in a wide range of applications, such as portable electronics and electric vehicles [4].

Having the most considerable potential as electrochemical energy storage systems, supercapacitors demonstrate a higher power density and longer cycle life than batteries and a greater energy density than conventional capacitors [5]. Supercapacitors can be classified into two types according to their charge storage mechanisms. The energy storage mechanisms of electrical double-layer capacitor originate from the separation of charges at the interface among the

Address correspondence to E-mail: qcao2000@163.com

electrode, electrolyte, and pseudocapacitor, which stores energy through reversible faradic redox reactions of electroactive species on the surface of the electrode [6]. The performance of supercapacitors significantly depends on the utilized electrode materials. Compared with other electrode materials, porous carbon materials, such as activated carbons [7], activated graphene [8], carbon nanotube [9], nano-onions [10], nanorods [11], carbon aerogel [12], and carbon nanocages [13], have been investigated extensively because of their satisfactory acid and alkali resistance, high specific capacitance, and high charge–discharge cycling stability. Scholars mostly argue that the hierarchical porosity of carbon facilitates the transfer of ions and electrons as well as the formation of an electrical double-layer structure [14]. The high graphitization degree of carbon materials likewise enhances the transfer of electrons. The methods for doping carbon materials with nitrogen, oxygen, or sulfur-containing compounds have also been explored to improve the surface wettability of carbon materials and to facilitate the access of electrolyte [15, 16]. However, the artificial introduction of these polar heteroatoms inevitably increases the cost of the final materials. The content of these heteroatoms in carbon materials can be increased with low cost by using the properties of the raw materials than the aforementioned doping methods. Accordingly, we select the mixture of coal-tar pitch (CTP) and sawdust (SD) as the precursor of carbon materials. CTP, which mainly contains polycyclic aromatic hydrocarbons, is a byproduct of the coking process of the coal industry. During carbonization, the graphitized structures that increase the conductivity of CTP are more easily formed than biomass. The carbonization yield contains significant proportions (50–60 %) of CTP [17]. SD contains a significant amount of microtubular bundles and a high oxygen content of approximately 47 wt%. The oxygen content of the resultant carbon material is significantly higher than that of CTP and biomass microtubular structures, thereby allowing the resultant carbon materials from SD to facilitate ion transportation [18]. Therefore, this study attempts for the first time to combine the advantages of CTP and SD by their co-carbonization to improve the electrochemical performance of the produced carbon materials. Experimental results show that the oxygen content of the resultant carbon material can reach 25 wt%, and the microtubular structure remains evident. After

activation, the prepared carbon material with well-developed microporosity possesses a high specific surface area (2224 m²/g) and a high micropore volume (88.17 vol.%). The as-prepared electrode exhibits an excellent cycling stability with a retention rate of 93 % after 7000 cycles and a favorable rate capability. The low raw material cost, easy preparation, and favorable electrochemical performance of the prepared carbon material demonstrate its potential as a favorable electrode material for supercapacitors. These findings provide a promising route for enhancing the added value of CTP and SD.

Experimental

Preparation of activated carbon materials

Figure 1 shows the schematic preparation and the three-electrode measuring equipment of tubular activated carbons. CTP (softening point of 120 °C) and SD from processed poplar wood were ground and screened through a 100-mesh sieve (149 μm) before use. These materials were mixed at different mass ratios (i.e., 0:10, 3:10, 5:10, and 7:10 for $m_{SD}:m_{CTP}$) in a motor stirrer at 150 °C and then cooled down to room temperature. Subsequently, the mixture was placed in a tube furnace and heated to 500 °C at a rate of (10 °C/min) under N₂ atmosphere (50 mL/min), and this temperature was maintained for 2 h. The co-carbonization products were ground into powder and mixed with KOH powder at a mass ratio of 1:3 (co-carbonization products: KOH powder). Afterward, the products were heated to 800 °C, and this temperature was maintained for 2 h. After

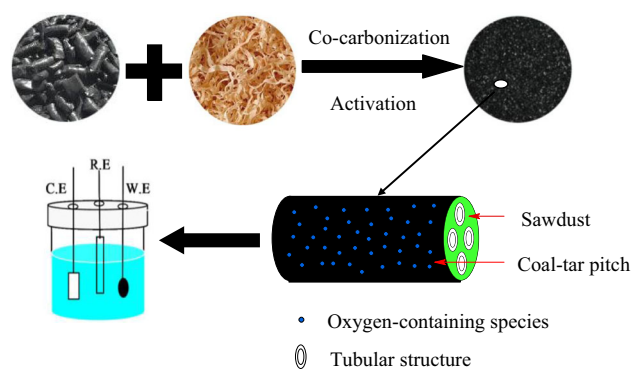
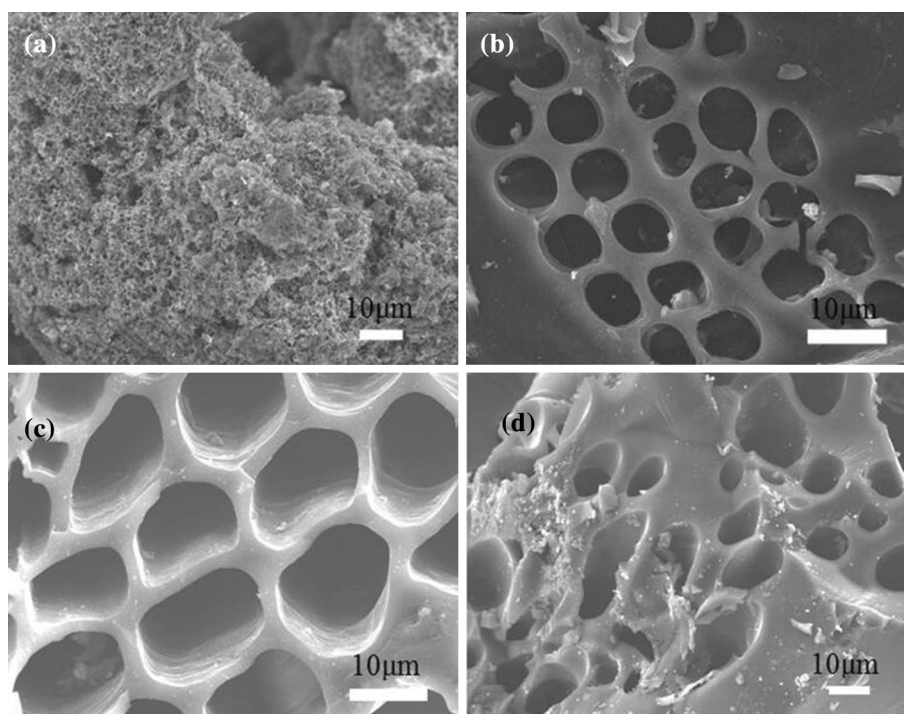


Figure 1 Schematic preparation and the three-electrode measuring equipment of tubular activated carbons.

Figure 2 FESEM images of resultant carbon materials: **a** AC–SD–0, **b** AC–SD–0.3, **c** AC–SD–0.5, and **d** AC–SD–0.7.



cooling, the activated carbon materials were neutralized with H_2SO_4 solution (1 mol/L) and washed with distilled water repeatedly until the pH of the filtrate reached 7. The cleaned samples were dried at 110°C for 12 h. The resultant activated carbon materials were denoted by AC–SD– x , where x is the mass ratio of SD:CTP.

Characterization methods

The morphology of the AC was characterized via a field emission scanning electron microscopy (FESEM) (JEOL.JSM-7001F). The pore distributions were measured using a Micromeritics ASAP 2020 analyzer, and the specific surface area was calculated using the Brunauer–Emmett–Teller (BET) plot of the nitrogen adsorption isotherm. The micropore volumes (V_{mic}) and total volumes (V_t) were estimated using the t-plot method. XPS was conducted using a Thermo ESCALAB 250 spectrometer with an Al $K\alpha$ radiation source to analyze the chemical bonding state and composition of the samples. The crystalline structures were determined using an X-ray diffractometer (D/max-2500) with a Cu $K\alpha$ radiation source and a scanning angle range of 5° – 80° . Electrochemical analysis was performed using a CHI660D electrochemical workstation that could perform CV, GCD, and EIS. The CV measurements were obtained at

sweep rates of 10, 20, 40, 60, 80, and 100 mV/s in the potential range from -1 to 0 V. The GCD measurements were conducted at scan rates of 0.5, 1, 2, 3, 4, and 5 A/g in the potential range from -1 to 0 V. The EIS measurements were performed with an amplitude of 5 mV over a frequency range of 10^{-2} – 10^5 Hz.

The specific capacitance (C in F/g) of a single electrode was obtained from the discharge curve as follows:

$$C = (I \cdot \Delta t) / (m \cdot \Delta V), \quad (1)$$

where I (A), Δt (s), ΔV (V), and m (g) denote the current density, discharge time, voltage change during discharge, and mass of activated carbon in the working electrode, respectively.

Preparation of the electrodes

A typical three-electrode system that comprises a working electrode, a platinum plate ($2 \times 2 \text{ cm}^2$) as a counter electrode, and a saturated calomel electrode as a reference electrode was used for measuring the electrochemical performance of the working electrode. The working electrode was prepared by mixing the AC powders with polytetrafluoroethylene binder and acetylene black at a mass ratio of 8:1:1 (AC:polytetrafluoroethylene binder:acetylene black). Nickel foam with a 1.6 mm thickness and 12 mm

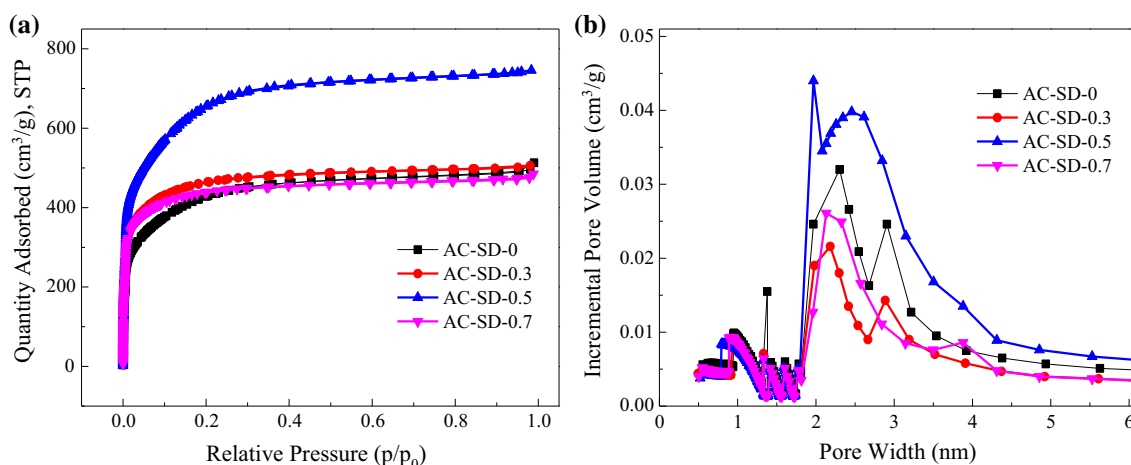


Figure 3 a Nitrogen adsorption and desorption isotherms and b pore size distributions of AC-SD-0, AC-SD-0.3, AC-SD-0.5, and AC-SD-0.7.

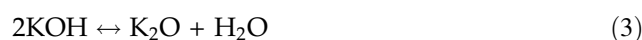
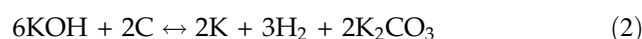
diameter was used as the current collector of the supercapacitor electrode. The mixture was then coated on the nickel foam substrate and pressed for 3 min at 10 MPa. The electrode was dried in an oven at 60 °C for 2 h. The electrochemical performance of the prepared electrode was investigated using a three-electrode experimental cell in a KOH solution (6 mol/L) with a CHI660D electrochemical workstation.

Results and discussion

Structural and morphological characterization

The porous structure of the prepared carbon materials was confirmed via FESEM. Figure 2a shows that the AC-SD-0 sample has a highly disordered pore network, whose morphology is similar to that observed among most ACs from CTP [19]. In this case, the migration speed of ion through the micropores becomes a rate-determining step, and the carbon materials exhibit a low specific capacitance [20]. As shown in Fig. 2b–d, the carbon materials inherit the pristine microtubules of SD upon its addition, thereby resulting in a tubular porous structure that provides a better channel for ion transfer than a microporous structure, which subsequently improves the specific capacitance of the electrode materials. The morphology of the microtubules varies as the proportion of SD increases further. The microtubules of AC-SD-0.3 (Fig. 2b) are smaller than those of AC-

SD-0.5 (Fig. 2c) because of the relatively high proportion of CTP, which adheres to the wall of the pristine microtubules of SD to a certain extent. A higher proportion of CTP can help form a layer of carbonized thin film on the surface of the interior of microtubules, which can weaken the reaction of KOH to microtubules because the reaction activity of carbonization matters from SD to KOH is higher than that of CTP. Given its higher proportion of SD, AC-SD-0.7 provides more microtubules than AC-SD-0.3 and AC-SD-0.5, which suggests that additional molten KOH may move into their interior and react, thereby creating an irregular tubular channel on the surface of holes [21]. Some corrosion reactions between the carbon matrix and KOH may occur as follows [22]:



A uniform microtubule structure is observed only in AC-SD-0.5 because of the appropriate ratio between CTP and SD. Given that the main components of CTP, such as polyaromatic hydrocarbon, are more stable than polysaccharide in biomass, such as SD, the proportions of both raw materials need to be controlled to improve the electrochemical properties of the ACs.

The isotherms of N₂ adsorption and desorption provide additional details on the specific surface area and pore structure of the produced samples (Fig. 3a,

Table 1 Porosity characteristics and carbon yield of the ACs

Samples	S_{BET} (m^2/g)	V_{t} (cm^3/g)	V_{mic} (cm^3/g)	$V_{\text{mic}}/V_{\text{t}}$	Pore width (nm)	Carbon yield (wt%)
AC–SD–0	1435	0.7938	0.6562	0.8267	2.21	32.45
AC–SD–0.3	1510	0.7823	0.7053	0.9016	2.07	29.03
AC–SD–0.5	2224	1.1538	1.0173	0.8817	2.08	27.50
AC–SD–0.7	1414	0.7499	0.6650	0.8868	2.12	23.73

b). Figure 3a shows that the isotherms of all samples exhibit a typical isotherm curve according to the IUPAC classification. The quantity of adsorbed N_2 rapidly approaches saturation level at a relative pressure below 0.05 and demonstrates a slightly upward slope in the medium relative pressure region. These results indicate the presence of a considerable number of micropores and a moderate number of mesopores, which characterize microporous materials [23]. An indistinct hysteresis loop also appears, to reflect the capillary condensation in the mesopores and this loop results from the collapse of the micropores during KOH activation [24]. AC–SD–0.5 has a wider knee and a higher N_2 adsorption capacity than the other three samples, thereby indicating the highly developed micropores of this sample.

The electrode materials for supercapacitors ideally must have a hierarchical porous structure that contains micropores (≤ 2 nm) for enhancing charge storage, mesopores (2–50 nm) for facilitating ion transfer, and macropores (≥ 50 nm) for providing ion-buffering reservoirs [25]. Figure 3b illustrates the AC pore size distributions obtained using the Horvath–Kawazoe and Barrett–Joyner–Halenda methods. Table 1 summarizes the porosity characteristics and carbon yields of the ACs. AC–SD–0.5 has the highest specific surface area ($2224 \text{ m}^2/\text{g}$) and pore volume ($1.1538 \text{ cm}^3/\text{g}$) among all samples under the same operating conditions, which indicates that the composition of the AC precursor significantly affects the porosity characteristics. A significantly high or low proportion of SD in the mixture is unfavorable for increasing the specific surface area of carbon materials. Another criterion for the assessment for electrode materials is the cost, which is related to the carbon yield of its precursor. Although the carbon yield decreases continuously as SD increases, the carbon yield from the CTP/SD precursor remains significantly higher than those from cocoa pod husk [26], straw pulping [27], and other biomass.

Table 2 Results of the elemental analyses on the precursors and typical AC

Precursor/sample	Elemental (wt%)				
	C	H	N	S	O_{diff}
CTP	93.48	4.79	1.0	0.56	0.17
SD	46.32	5.94	0.35	0.11	47
AC–SD–0.5	73.10	1.06	0.28	0.31	25

Table 2 presents the results of the elemental analyses on the precursors and AC–SD–0.5. The oxygen content of AC–SD–0.5 reaches 25 wt%, which is much higher than that of AC–SD–0 (0.17 wt%). These results indicate that adding the raw material SD can increase the oxygen content in carbon materials. Recent studies show that the existence of heteroatom oxygen in the carbon skeleton has multiple roles in the electrochemical performance of carbon materials [28]. The distribution of oxygen-containing species on the surface of carbon materials is further observed via X-ray photoelectron spectroscopy (XPS), as shown in Fig. 4a, b. Both AC–SD–0 and AC–SD–0.5 present the binding energy peaks of oxygen atoms at approximately 533.4, 532.2, and 531.3 eV, which correspond to the –OH, C=O, and C–O groups [29], respectively. Table 3 lists the oxygen contents on the surfaces of the two AC samples (i.e., AC–SD–0 and AC–SD–0.5). The oxygen content demonstrates an approximately twofold increase from 9.78 % for AC–SD–0 to 19.40 % for AC–SD–0.5, with the addition of SD. The oxygen functionalities contribute to pseudocapacitance through the quinone/hydroquinone redox pair [30]. The oxygen contents on the surface and in the body also significantly differ, with the latter being higher than the former. This phenomenon may be ascribed to the surface energy of carbon. Some errors may result from the use of the subtraction method in the calculation, which means that some non-oxygen-containing components have also been considered. The deconvolution of the C1s XPS spectrum of AC–SD–0 and AC–SD–0.5 (Fig. 4c, d) reveals three peaks

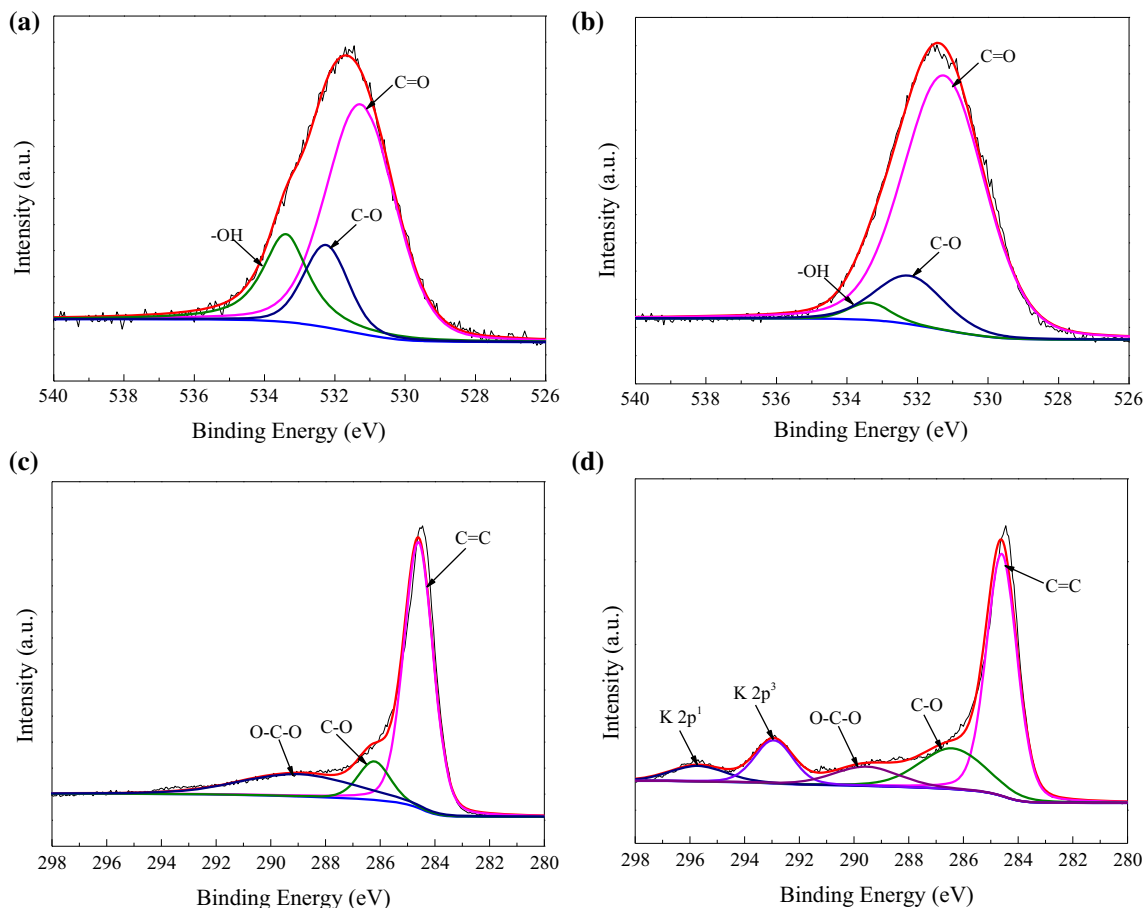


Figure 4 XPS spectra of the O1 s region for **a** AC-SD-0, **b** AC-SD-0.5 and the C1 s region for **c** AC-SD-0, **d** AC-SD-0.5.

Table 3 XPS analyses of AC-SD-0 and AC-SD-0.5

Samples	XPS analysis (atom %)		
	C	N	O
AC-SD-0	88.48	1.74	9.78
AC-SD-0.5	78.91	1.69	19.40

at 284.6, 286.4, and 289.0 eV, which belong to the C = C, C-O, and O-C-O groups, respectively [31]. This finding confirms the presence of activated carbon in the samples. The other two peaks at 292.9 and 295.7 eV are related to the formation of K 2p³ and K 2p¹ hybridized bonds, respectively.

Figure 5 shows the two broad peaks at approximately 23.8° and 44.6° in the XRD patterns, and these peaks can be attributed to the (002) and (100) diffraction peaks, respectively. The peak of AC-SD-0.5 has a slightly higher intensity than those of the other samples, thereby indicating its enhanced graphitization degree. This enhancement improves

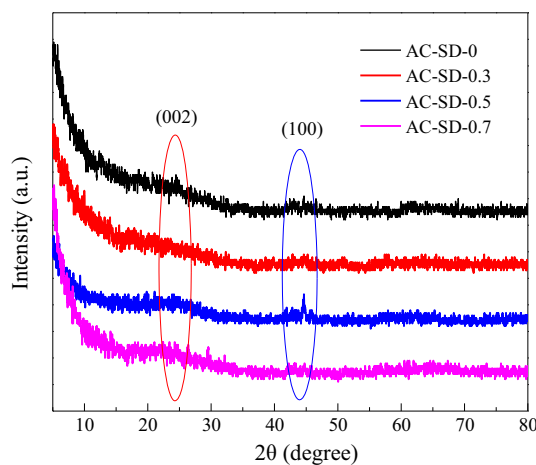


Figure 5 XRD patterns of AC-SD-0, AC-SD-0.3, AC-SD-0.5, and AC-SD-0.7.

both the rate of electron transfer and the chemical performance of the carbon materials. These results are consistent with the FESEM results.

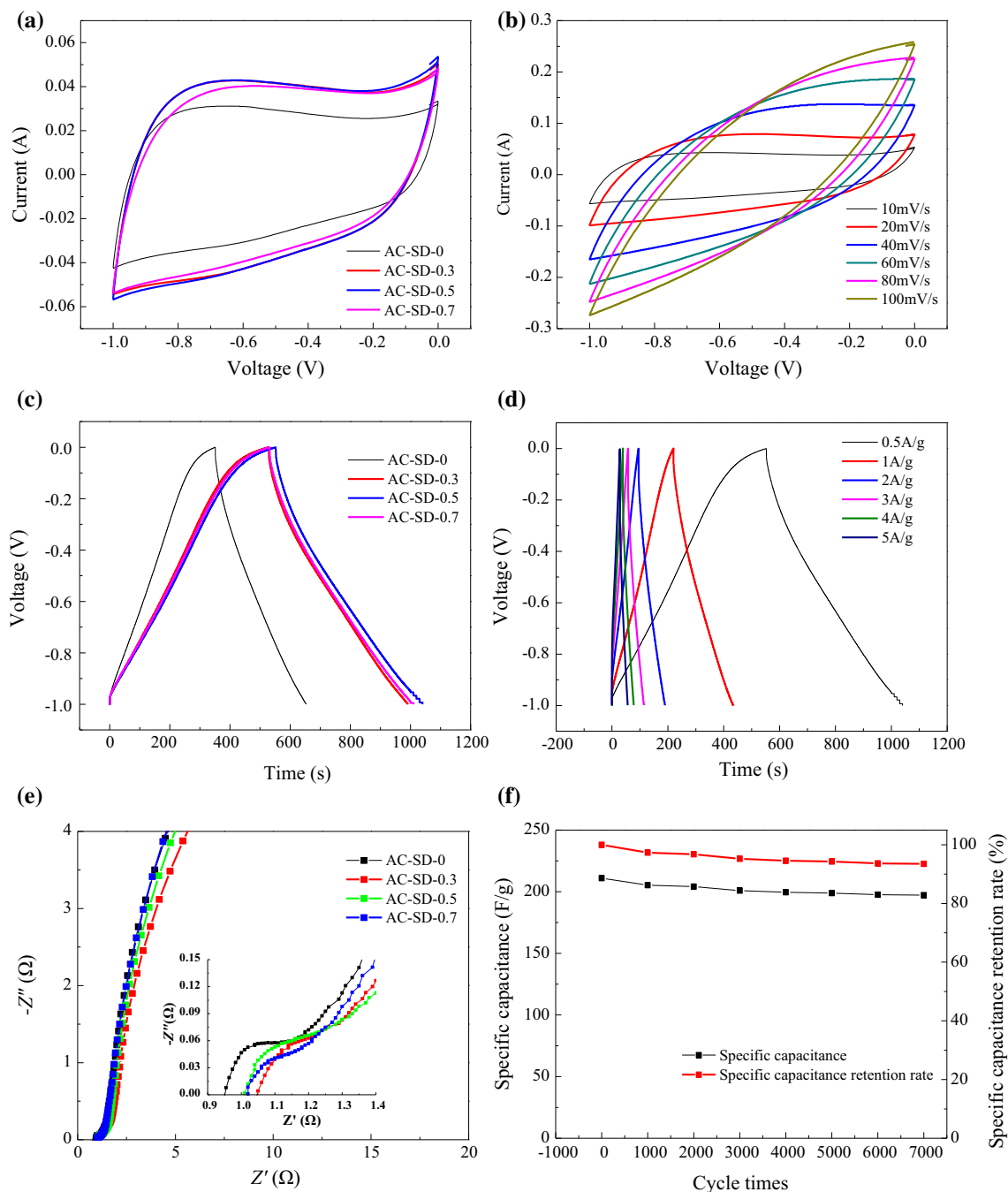


Figure 6 Electrochemical performances of the prepared AC electrodes: **a** CV curves of AC-SD-0, AC-SD-0.3, AC-SD-0.5, and AC-SD-0.7 at a scan rate of 10 mV/s; **b** CV curves of AC-SD-0.5 at scan rates ranging from 10 to 100 mV/s; **c** GCD curves of AC-SD-0, AC-SD-0.3, AC-SD-0.5, and AC-SD-0.7

at a current density of 0.5 A/g; **d** GCD curves of AC-SD-0.5 at a current density ranging from 0.5 to 5 A/g; **e** Nyquist plots in the frequency range of 10^{-2} – 10^5 Hz; **f** specific capacitance and cycling stability of the AC-SD-0.5 electrode at a current density of 2 A/g.

Electrochemical characterization

Figure 6a shows the cyclic voltammetry (CV) curves of the four AC samples at a scan rate of 10 mV/s. All curves exhibit a quasi-rectangular shape without

evident oxidation/reduction peaks, which reflects the characteristic of an electrical double-layer capacitor. This result is consistent with those produced by using tobacco rods as precursors [32]. The CV curve of AC-SD-0 has the smallest area among all CV curves of

Table 4 Specific capacitance of the four AC samples at different current densities

Samples	Specific capacitance (F/g)					
	0.5 A/g	1 A/g	2 A/g	3 A/g	4 A/g	5 A/g
AC–SD–0	156	142	132	125	119	111
AC–SD–0.3	239	214	200	191	182	176
AC–SD–0.5	251	225	211	199	194	186
AC–SD–0.7	245	221	206	195	184	183

the AC samples because of the slow ionic transport rate in the micropores [33], which suggests the low specific capacitance of AC–SD–0. By contrast, the CV curve of AC–SD–0.5 has the largest area that can be ascribed to the desirable porous structure and large specific surface area of this sample, which in turn can be attributed to the moderate addition of SD. Figure 6b shows the CV curves of AC–SD–0.5 at scan rates that range from 10 to 100 mV/s. As the scan rate increases, the profile deviates severely from the rectangular shape. This phenomenon is mainly attributed to the existence of numerous micropores in AC–SD–0.5, in which the electrolyte ion has a slow migration speed. Therefore, the current takes a long time to reach a stable value. However, the curves of AC–SD–0.5 have a quasi-rectangular shape with no obvious distortions and are symmetrical even at a high sweep rate of 100 mV/s, which indicates that this AC sample still belongs to the electrical double-layer capacitor type.

Figure 6c shows the galvanostatic charge/discharge (GCD) curves. The charge and discharge branches are not completely symmetrical even if the entire shape is nearly linear, which suggests the existence of a low pseudocapacitance except for the typical electrical double-layer capacity. A comparison between the charge/discharge times of the AC samples reveals that the charge/discharge times of AC–SD–0.5 become longer than that of AC–SD–0 after SD is added to CTP. The GCD curves of AC–SD–0.5 are investigated at current densities that range from 0.5 to 5 A/g as shown in Fig. 6d. All curves of AC–SD–0.5 at various current densities are quasi-triangular and symmetrical, which suggests excellent capacitive behavior and electrochemical reversibility. These findings are consistent with the CV results. The curve straightens as the current density increases and such change is driven by the presence of less active sites

that contact the electrolyte at a high current density such that fewer heteroatoms are involved in the reaction. Nevertheless, a minimal difference still exists. For example, the voltage values deviate from the straight line when the charge approaches the equilibrium at the beginning of the discharge process. This result may be attributed to the low pseudocapacitance that results from the oxygen-containing species.

Table 4 summarizes the capacitance values that are calculated from the GCD curves at current densities ranging from 0.5 to 5 A/g for all ACs. The specific capacitance of AC–SD–0.5 can reach a maximum of 251 F/g and maintain a value as high as 186 F/g even at a high current loading of 5 A/g. The specific capacitance values of the ACs with SD are significantly higher than those of AS–SD–0 and of other similar porous carbon electrode materials [31, 34]. This finding may be attributed to the large specific surface area, well-developed tubular structure, and multiple oxygen functionalities on the surface of the carbon materials that are obtained from SD/CTP co-carbonization, which can be easily realized in practice.

Figure 6e shows the electrochemical impedance spectroscopy (EIS) results of the AC electrode materials. The Nyquist plots can be divided into three parts, namely, a semicircle in the high frequency, a line with an approximately 45° slope in the middle frequency, and a linear region in the low frequency. The first intersection that points toward the real axis is called the solution resistance (R_s), which includes the resistance of the electrolyte, the intrinsic resistance of the active material, and the contact resistance at the interface between the active electrode material and the current collector [35]. The magnified data in the high-frequency region of Fig. 6e inset show that the R_s of AC–SD–0, AC–SD–0.3, AC–SD–0.5, and AC–SD–0.7 are approximately 0.93, 1.04, 0.98, and 0.99 Ω , respectively. Although the R_s of AC–SD–0.5 is higher than that of AC–SD–0, this value remains considerably lower than those of other ACs under similar testing conditions. Such difference may be attributed not only to the excellent tubular structure of AC–SD–0.5, which promotes ion transfer, but also to its oxygen-containing components, which improve surface wettability and electrical conductivity. A nearly vertical line is also produced by the Warburg impedance, thereby indicating the favorable capacitive performance of AC–SD–0.5.

Figure 6f shows the cycling stability of AC–SD–0.5 as an electrode material. AC–SD–0.5 demonstrates an excellent long cycling stability with a 93 % retention rate and a high specific capacitance of as high as 197 F/g even after exceeding 7000 cycles at 2 A/g, which indicate that the charge/discharge process is highly reversible and that AC–SD–0.5 possesses an excellent long cycling durability.

Conclusions

High-surface area-activated carbons are successfully prepared via CTP–SD co-carbonization followed by KOH activation. The oxygen content of carbonizing 67 % CTP and 33 % SD is 25 wt% higher than that derived by carbonizing CTP alone. The graphitization degrees and carbon yields of the carbon materials obtained by co-carbonization also increase relative to SD-only carbonization. The microtubular structures of ACs are inherited from the structural characteristic of SD. Moreover, the diameter of the microtubules can be adjusted by adjusting the proportion of CTP in the mixture. Therefore, the AC samples combine the advantages of CTP and SD. At 800 °C, the typical AC (i.e., AC–SD–0.5) has a carbon yield of 27.50 %, which is significantly higher than the carbon yields of other biomass materials. This AC also has a BET surface area of 2224 m²/g. As an electrode material for supercapacitors, AC–SD–0.5 exhibits a high specific capacitance of 251 F/g at a current density of 0.5 A/g, a favorable rate capability with a retention of 74 % at 5 A/g, and an excellent cycling stability with 93 % retention rate over 7000 cycles at 2 A/g in KOH electrolyte. In terms of its potential practical applications in supercapacitors, the electrode materials AC–SD–0.5 possess many advantages, such as low cost, easy processability into large or small devices, facile scale-up preparation, and excellent energy storage performance. Therefore, high-performance and low-cost electrode materials must be produced for supercapacitors.

Acknowledgements

The authors are very grateful for the financial support of the National Natural Science Foundation of China NSFC (Grant No. 51174144).

Compliance with ethical standards

Conflict of interest The authors declare that they have no conflict of interest.

References

- [1] Hu ZX, Li SS, Cheng PP, Yu WD, Li RC, Shao XF, Lin WR, Yuan DS (2016) N, P-co-doped carbon nanowires prepared from bacterial cellulose for supercapacitor. *J Mater Sci* 51:2627–2633. doi:10.1007/s10853-015-9576-x
- [2] Wang HL, Mitlin D, Ding J, Li Z, Cui K (2016) Excellent energy-power characteristics from a hybrid sodium ion capacitor based on identical carbon nanosheets in both electrodes. *J Mater Chem A* 4:5149–5158
- [3] Lotfabad EM, Kalisvaart P, Kohandehghan A, Karpuzov D, Mitlin D (2014) Origin of non-SEI related coulombic efficiency loss in carbons tested against Na and Li. *J Mater Chem A* 2:19685–19695
- [4] Chen JZ, Xu JL, Zhou S, Zhao N, Wong CP (2016) Nitrogen-doped hierarchically porous carbon foam: a free-standing electrode and mechanical support for high-performance supercapacitors. *Nano Energy* 25:193–202
- [5] Wang HL, Li Z, Mitlin D (2014) Tailoring biomass-derived carbon nanoarchitectures for high-performance supercapacitors. *ChemElectroChem* 1:332–337
- [6] Yao F, Pham DT, Lee YH (2015) Carbon-based materials for lithium-ion batteries, electrochemical capacitors, and their hybrid devices. *ChemSusChem* 8:2284–2311
- [7] Kim MH, Kim KB, Park SM, Roh KC (2016) Hierarchically structured activated carbon for ultracapacitors. *Sci Rep* 6:21182–21201
- [8] Song YF, Yang J, Wang K, Haller S, Wang YG, Wang CX, Xia YY (2016) In-situ synthesis of graphene/nitrogen-doped ordered mesoporous carbon nanosheet for supercapacitor application. *Carbon* 96:955–964
- [9] Dubal DP, Chodankar NR, Caban-Huertas Z, Wolfart F, Vidotti M, Holze R, Lokhande CD, Gomez-Romero P (2016) Synthetic approach from polypyrrole nanotubes to nitrogen doped pyrolyzed carbon nanotubes for asymmetric supercapacitors. *J Power Sources* 308:158–165
- [10] Zeigerab M, Jäckelab N, Mochalin VN, Presser V (2016) Review: carbon onions for electrochemical energy storage. *J Mater Chem* 4:3172–3196
- [11] Wang LX, Deng D, Salley SO (2015) Facile synthesis of 3-D composites of MnO₂ nanorods and holey graphene oxide for supercapacitors. *J Mater Sci* 50:6313–6320. doi:10.1007/s10853-015-9169-8

- [12] Li C, Yang X, Zhang G (2015) Mesopore-dominant activated carbon aerogels with high surface area for electric double-layer capacitor application. *Mater Lett* 161:538–541
- [13] Xie K, Qin X, Wang X, Wang Y, Tao H, Wu Q, Yang L, Hu Z (2012) Carbon nanocages as supercapacitor electrode materials. *Adv Mater* 24:347–352
- [14] Yue Y, Liang H (2015) Hierarchical micro-architectures of electrodes for energy storage. *J Power Sources* 284:435–445
- [15] Huang HF, Lei CL, Luo GS, Cheng ZZ, Li GX, Tang SL, Du YW (2016) Facile synthesis of nitrogen-doped graphene on Ni foam for high-performance supercapacitors. *J Mater Sci* 51:6348–6356. doi:10.1007/s10853-016-9331-6
- [16] Ding J, Li Z, Cui K, Boyer S, Karpuzov D, Mitlin D (2016) Heteroatom enhanced sodium ion capacity and rate capability in a hydrogel derived carbon give record performance in a hybrid ion capacitor. *Nano Energy* 23:129–137
- [17] Cao Q, Guo L, Dong Y, Xie X, Jin L (2015) Autocatalytic modification of coal tar pitch using benzoyl chloride and its effect on the structure of char. *Fuel Process Technol* 129:61–66
- [18] Liu XR, Zheng MT, Xiao Y, Yang YH, Yang LF, Liu YL, Lei BF, Dong HW, Zhang HR, Fu HG (2013) Microtube bundle carbon derived from paulownia sawdust for hybrid supercapacitor electrodes. *ACS Appl Mater Interfaces* 5:4667–4677
- [19] Wang L, Wang J, Jia F, Wang C, Chen M (2013) Nanoporous carbon synthesised with coal tar pitch and its capacitive performance. *J Mater Chem A* 1:9498–9507
- [20] Li L, Wang X, Wang S, Cao Z, Wu Z, Wang H, Gao Y, Liu J (2015) Activated carbon prepared from lignite as supercapacitor electrode materials. *Electroanalysis* 28:243–248
- [21] Tseng RL, Tseng SK (2005) Pore structure and adsorption performance of the KOH-activated carbons prepared from corncob. *J Colloid Interf Sci* 287:428–437
- [22] Raymundo-Piñero E, Azaña P, Cacciaguerra T, Cazorla-Amorós D, Béguin F (2005) KOH and NaOH activation mechanisms of multiwalled carbon nanotubes with different structural organisation. *Carbon* 43:786–795
- [23] Shu K, Wang C, Li S, Zhao C, Yang Y, Liu H, Wallace G (2015) Flexible free-standing graphene paper with interconnected porous structure for energy storage. *J Mater Chem A* 3:4428–4434
- [24] Zheng Z, Gao Q, Jiang J (2010) High hydrogen uptake capacity of mesoporous nitrogen-doped carbons activated using potassium hydroxide. *Carbon* 48:2968–2973
- [25] Gong S, Cao Q, Jin L, Zhong C, Zhang X (2015) Electrodeposition of three-dimensional Ni(OH)₂ nanoflakes on partially crystallized activated carbon for high-performance supercapacitors. *J Solid State Electrochem* 20:619–628
- [26] Cruz G, Pirilä M, Huuhtanen M, Carrión L, Alvarenga E, Keiski RL (2012) Production of activated carbon from cocoa (*Theobroma cacao*) pod husk. *J Civil Environ Eng* 2:1–6
- [27] Jin XJ, Yu ZM, Wu Y (2012) Preparation of activated carbon from lignin obtained by straw pulping by KOH and K₂CO₃ chemical activation. *Cellulose Chem Technol* 46:79–85
- [28] Zhao L, Baccile N, Gross S, Zhang Y, Wei W, Sun Y, Antonietti M, Titirici MM (2010) Sustainable nitrogen-doped carbonaceous materials from biomass derivatives. *Carbon* 48:3778–3787
- [29] Zhao Q, Wang X, Xia H, Liu J, Wang H, Gao J, Zhang Y, Liu J, Zhou H, Li X (2015) Design, preparation and performance of novel three-dimensional hierarchically porous carbon for supercapacitors. *Electrochim Acta* 173:566–574
- [30] Zhao YQ, Lu M, Tao PY, Zhang YJ, Gong XT, Yang Z, Zhang GQ, Li HL (2016) Hierarchically porous and heteroatom doped carbon derived from tobacco rods for supercapacitors. *J Power Sources* 307:391–400
- [31] Muniandy L, Ng EP, Adam F, Mohamed AR, Jose R, Chong KF (2016) High surface area activated carbon from rice husk as a high performance supercapacitor electrode. *Electrochim Acta* 192:110–119
- [32] Chen LF, Zhang XD, Liang HW, Kong M, Guan QF, Chen P, Wu ZY, Yu SH (2012) Synthesis of nitrogen-doped porous carbon nanofibers as an efficient electrode material for supercapacitors. *ACS Nano* 6:7092–7102
- [33] Fang BZ, Kim JH, Kim MS, Bonakdarpour A, Lam A, Wilkinson DP, Yu JS (2012) Fabrication of hollow core carbon spheres with hierarchical nanoarchitecture for ultrahigh electrical charge storage. *J Mater Chem* 22:19031–19038
- [34] Zhang XS, Yan PT, Zhang RJ, Jin JL, Xu J (2016) Fabrication of graphene and core-shell activated porous carbon-coated carbon nanotube hybrids with excellent electrochemical performance for supercapacitors. *Int J Hydrog Energ* 41:6394–6402
- [35] Barzegar F, Bello A, Momodu D, Madito MJ, Dangbegnon J, Manyala N (2016) Preparation and characterization of porous carbon from expanded graphite for high energy density supercapacitor in aqueous electrolyte. *J Power Sources* 309:245–253